

# An explanation of the large PGA value of 2013 $M_S7.0$ Lushan earthquake at 51BXD station through topographic analysis

Zhijun Dai · Xiaojun Li

Received: 13 September 2013 / Accepted: 19 November 2013 / Published online: 8 January 2014

© The Seismological Society of China, Institute of Geophysics, China Earthquake Administration and Springer-Verlag Berlin Heidelberg 2014

**Abstract** In  $M_S7.0$  Lushan earthquake, a large amount of strong ground motion recordings were collected. In this paper, we analyze the recordings carefully. The abnormality of ground motion recordings is identified through a log linear regression. In the station of 51BXD, the PGA value has exceeded 1 g, which is the biggest peak ground acceleration (PGA) value obtained from all recordings in this earthquake. The log linear relation shows the PGA value in this station is abnormally large. As this station is located on the footage of a hill, the topographic amplification factor is explored in order to explain this abnormality. Through 3D numerical modeling using spectral element method with transmitting boundary conditions, the amplification factor is quantized. In this station, the topographic amplification is highly polarized in the direction of East–West which agrees with the empirical recordings. This research result suggests us in future directionality of topographic amplification should be considered in the aseismic design.

**Keywords** Strong ground motion · Topographic amplification · Ground motion directionality

## 1 Introduction

A large amount of strong ground motion recordings were collected from the  $M_S7.0$  Lushan earthquake of 20 April

2013. These data provide us new insights on the amplification of site conditions.

Previous research mainly focused on the amplification of soil profiles. The key parameter associated with the soil profile amplification is the shear-wave impedance. As the density of soil profiles varies less than shear-wave velocity and the shear-wave impedance is the product of the soil density with the shear-wave velocity, the average shear-wave velocity.

Previous works have shown that the topographic features, such as cliffs and ridges give significant amplifications, but these amplifications are less significant than the amplifications by soil profiles (Hartzell et al. 1994; Spudich et al. 1996; Bouchon et al. 1996; Assimaki et al. 2005; Hough et al. 2010). In recent years research, the topographic data are also correlated with  $V_{S30}$  as a proxy for site conditions (Iwahashi et al. 2010; Yong et al. 2012). In this paper, we find evidence that the amplification by topographic features plays an important role to the recorded strong ground motions. Also, many localized severe damages are attributed to the topographic amplifications, such as 2010  $M7.0$  Haiti earthquake (Hough et al. 2010), 2011 Christchurch earthquake (Kaiser et al. 2013).

To quantify the topographic effects, theoretical computation is a powerful tool to check the amplification by a variety of terrain surfaces. Tsaur (2011) studied the SH wave propagation behavior through the semi-elliptic convex topography. Zhang et al. (2012a, b) provided the solution for V-shaped canyon, and similarly the U-shaped canyon (Gao et al. 2012) and circular sectorial canyon (Chang et al. 2013) were investigated systematically.

In the theoretical analysis, some simple shapes could employ analytic solutions to get the amplification effects (Tsaur 2011). For irregular 3D modeling, finite element method or spectral element method is preferred (Komatitsch and Vilotte 1998; Komatitsch and Tromp 1999).

Z. Dai · X. Li (✉)  
Institute of Geophysics, China Earthquake Administration,  
100081 Beijing, China  
e-mail: beerli@vip.sina.com

Z. Dai  
e-mail: dzj@cea-igp.ac.cn

In this study, we first analyze the strong ground motion recordings in brief and the abnormality on PGA value is focused. After that, the topographic amplification for 51BXD station is investigated in detail. Then we give some suggestions based on our analysis.

### 2 An analysis of the strong ground motion recordings

First, we explore the PGA values for each station. Table 1 shows ground motion measures for each station. In the table, the PGA or PGV value is the max absolute value over all horizontal orientations which are rotated from two horizontal components. They are peak values over all horizontal orientations for each recording. For the PGV computation, baseline drift is corrected for 51QLY station to get accurate PGV value. As the PGA value is generally attenuated exponentially by epi-distance, the relation between distance and PGA is fitted by the following linear relation

$$\log(\text{PGA}) = c_1 \log(\text{epi-distance}) + c_2. \tag{1}$$

Then the prediction error by the linear relation (1) is computed with the formula

$$\text{Err}_{\text{PGA}} = \frac{\text{PGA}_{\text{recorded}} - \text{PGA}_{\text{fitted}}}{\max\{\text{PGA}_{\text{fitted}}, \text{PGA}_{\text{recorded}}\}}. \tag{2}$$

**Table 1** Ground motion measures for each station

| ID | Station name | Epi-distance (km) | PGA (Gal) | PGV (cm/s) |
|----|--------------|-------------------|-----------|------------|
| 1  | 51BXD        | 22.23             | 1031.70   | 25.05      |
| 2  | 51YAM        | 24.12             | 402.92    | 13.38      |
| 3  | 51BXY        | 24.32             | 432.89    | 13.87      |
| 4  | 51BXM        | 30.90             | 388.49    | 19.07      |
| 5  | 51QLY        | 30.90             | 325.72    | 12.93      |
| 6  | 51LSF        | 34.61             | 409.74    | 16.26      |
| 7  | 51PJD        | 39.97             | 218.52    | 14.40      |
| 8  | 51YAL        | 48.36             | 285.00    | 10.87      |
| 9  | 51KDZ        | 80.00             | 33.33     | 2.22       |
| 10 | 51DJZ        | 96.80             | 82.07     | 2.98       |
| 11 | 51HYY        | 96.86             | 225.12    | 6.14       |
| 12 | 51PXZ        | 101.63            | 14.31     | 1.78       |
| 13 | 51KDT        | 101.73            | 83.59     | 2.12       |
| 14 | 51CDZ        | 110.62            | 76.51     | 3.56       |
| 15 | 51LSL        | 117.64            | 8.34      | 0.20       |
| 16 | 51GLQ        | 145.72            | 20.34     | 1.32       |
| 17 | 51MCL        | 159.49            | 4.74      | 0.28       |
| 18 | 51MNV        | 179.90            | 58.61     | 2.95       |
| 19 | 51AXT        | 188.87            | 21.57     | 1.25       |
| 20 | 51BCD        | 196.84            | 15.43     | 1.15       |
| 21 | 51DFT        | 197.75            | 4.74      | 0.76       |

Figure 1 shows the recorded PGA value against the epi-distance of each station and the fitted line by the recorded data. In the data fitting, only epi-distance less than 200 km is used for the regression. From the general trend of the data, it shows that the intrinsic relation between PGA and epi-distance is captured in general by the linear relation (1). Some large deviations from the fitting line are attributed to a variety of factors influencing the intensity of ground motions, including rupture process, basin effect, site condition, and topograph shape.

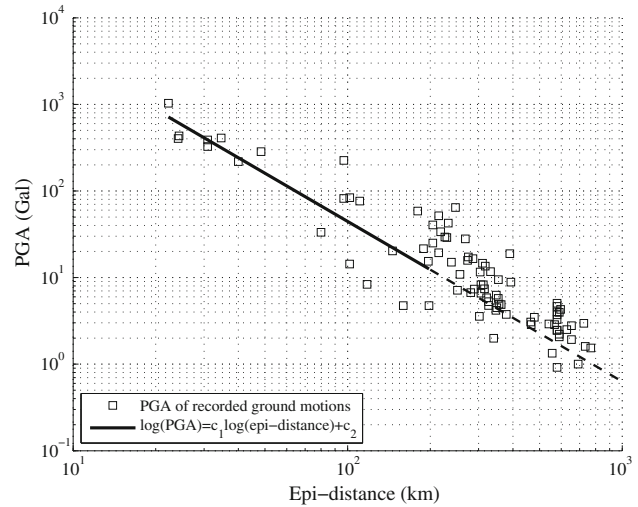


**Fig. 1** The recorded PGA value against the epi-distance of each station and the fitted line by the recorded data. In the data fitting, only epi-distance less than 200 km is used for the regression. The dashed line extends from the solid line for distance over 200 km

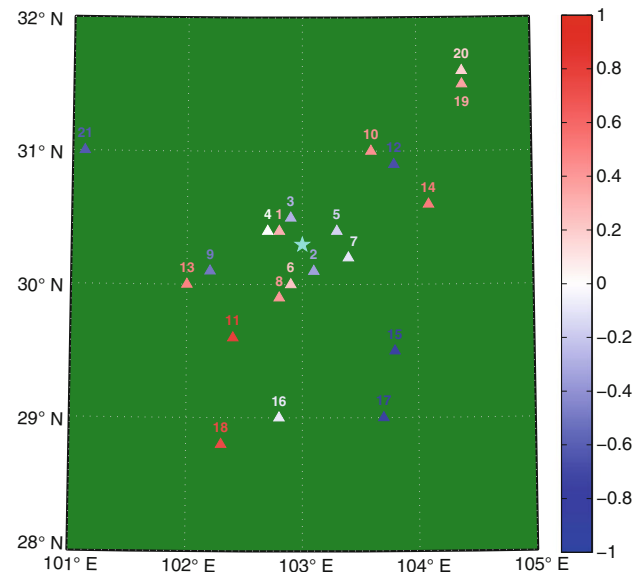


**Fig. 2** Spatial distribution for the fitting error between the recorded PGA value and the fitted PGA value. The cyan pentacle pentagram is the epicenter of the  $M_{5.70}$  Lushan earthquake

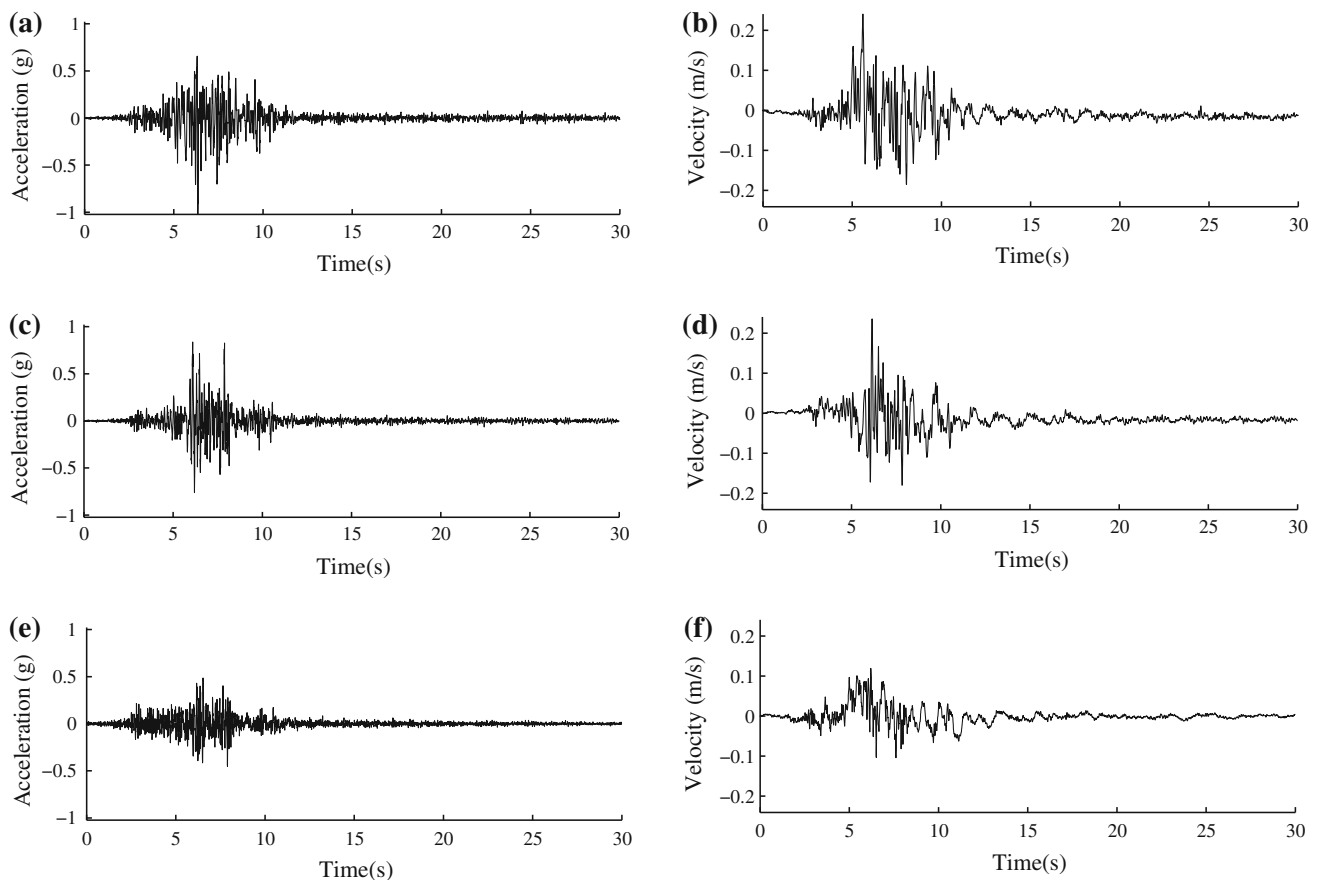


**Fig. 3** Acceleration and velocity time series for station 51BXD. **a** Acceleration, EW component. **b** Velocity, EW component. **c** Acceleration, NS component. **d** Velocity, NS component. **e** Acceleration, UD component. **f** Velocity, UD component

Figure 2 shows the error for each station. In each station location, the station ID number is shown.

Some PGA values of several stations are significantly larger than fitted value, and some others are significantly smaller than fitted value. The spatial distribution for this fitting abnormality is quite irregular. Some abnormality is obvious in the map. For example, PGA value in 51HYY station is 225.1220 Gal. This station is located in Hanyuan county (51HYY, epicenter distance: 96.861 km). For the station of (51PXZ) in Pixian county, the PGA value is very small, but its epi-distance approaches to the epi-distance of 51HYY station. This abnormality is mainly due to the sediment-induced amplification in Hanyuan county, which is also observed in 2008 *M*8.0 Wenchuan earthquake.

In the northwest region of the earthquake, three near stations have significantly different errors. As the after-shocks are mainly focused on Shuangshi–Dachuan fault, and the fault direction is from northeast to the southwest. From the map, it shows that the stations with ID 1, 3, and 4 are near each other, but the fitting errors are significantly different. Station with ID 1 has the largest PGA value among all stations. In this paper, we will try to answer why

the PGA value in this station is significantly larger than other stations.

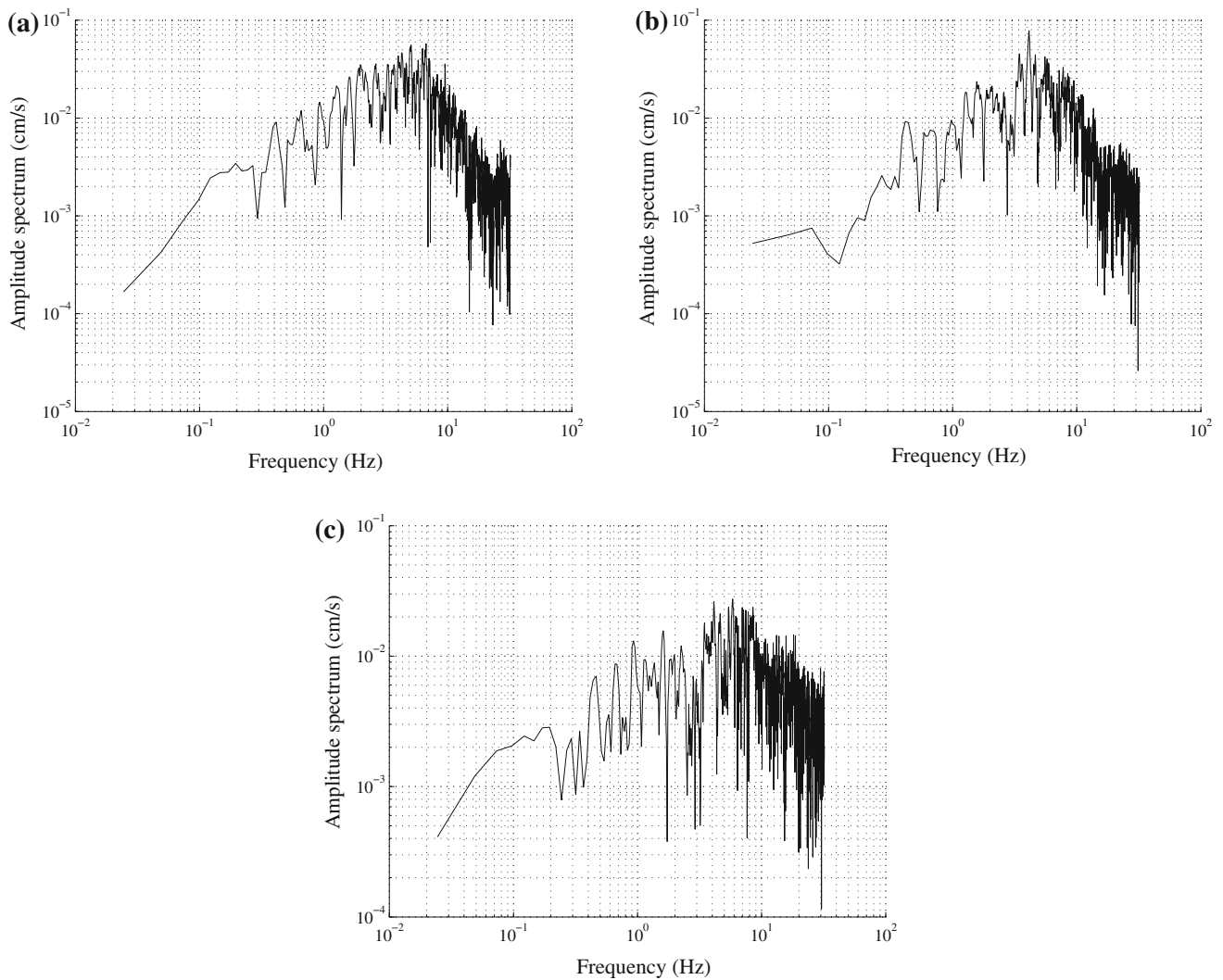
Figure 3 shows the acceleration and velocity time series for station 51BXD.

Figure 4 shows the Fourier spectra of the above recording. It clearly shows the energy of mainly focused from 1 to 10 Hz, and has peak value around 4 Hz.

Figure 5 shows the response spectra of this recording. The peak response for the response spectra is focused between 9 and 10 Hz.

### 3 Topographic amplification

We choose the location of this station as the center of region of interest. The 51BXD station is located at 30.4 N 102.8 W. The topographic data of this region is obtained from SRTM. The data file around this region is *srtm\_57\_06.zip*. Since the mesh of spectral element method (SEM) needs Cartesian coordinates, we convert the topography file from (longitude/latitude/elevation) to UTM (X/Y/Z) coordinates. The original data resolution is about



**Fig. 4** Fourier spectra for the acceleration time series. **a** Spectrum for the EW component, **b** spectrum for the NS component, **c** spectrum for the UD component

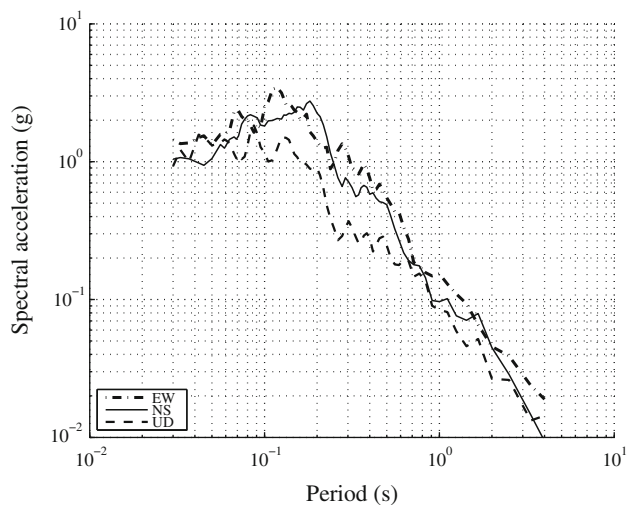


**Fig. 5** Response spectra for the acceleration time series of EW, NS, and UD components with damping ratio 5 %

90 m per point, and we sampled the data with 60 m per grid.

Figure 6 shows the topographic site condition of 51BXD station. The numerical simulation to quantify the topographic amplification will be carried out in this area. The area is  $600 \text{ m} \times 600 \text{ m}$ . In order to perform the simulation of 3D wave propagation, we set the depth of the simulated region be 300 m. Each element is a  $60 \text{ m} \times 60 \text{ m} \times 60 \text{ m}$  hexahedral. As we use SEM for the formulation, each element is further divided into  $N^3$  subelements and we set  $N = 5$ . The total grid points are  $51 \times 51 \times 26$ . For a wave with the wavelength is 60 m, the SEM formulation has five sample points per wavelength. Therefore, the simulation could resolve well for the wavelength as short as 60 m.

In the numerical modeling analysis, the soil profile is set homogeneous to avoid the complex coupling of soil amplification and topographic amplification. The soil

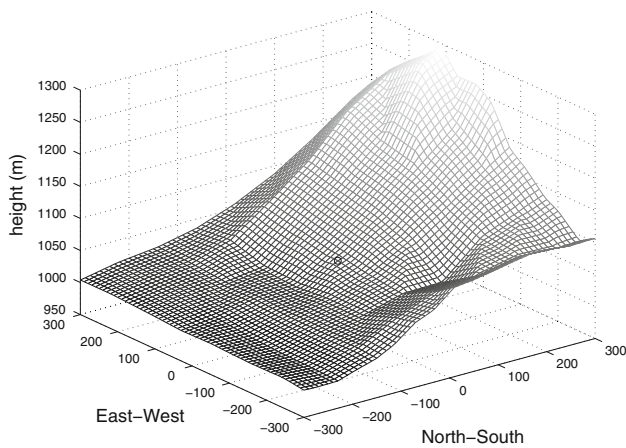


**Fig. 6** Topographic surface of 51BXD station. The station is in the center of the surface with an area 600 m × 600 m

properties are set according to the Crust 1.0 model. The shear-wave velocity is  $v_s = 1070$  m/s, and the soil density is  $\rho = 2110$  kg/m<sup>3</sup>. This shear-wave velocity makes our simulation could resolve well for the frequency up to  $f_{max} = v_s/\lambda_{min} = 1070/60 = 17.8$  Hz.

We excite the numerical model by two vertically propagating plane S-waves separately, which are polarized in the East–West and North–South directions, respectively. The excited time series on displacement  $u$  is the function of Ricker type

$$u(t) = [1 - 2(\pi f_p(t - t_0))^2] \exp(-(\pi f_p(t - t_0))^2), \quad (3)$$

where  $f_p$  is the dominant frequency of this wave, and  $t_0$  is a time shift parameter such that initial displacement approaches zero. We set  $f_p = 2$  Hz and  $f_p = 8$  Hz such that

the amplification factor around 0.2–5.5 Hz and 2–15 Hz could be resolved well.

The input acceleration time series come from the double differentiation of (3). Figures 7 and 8 show the input acceleration time series at the bottom of the numerical model and the output time series at the station for  $f_p = 2$  Hz and  $f_p = 8$  Hz, respectively. For  $f_p = 2$  Hz, the peak acceleration for the excitation of North–South direction is 171.68 Gal and is 397.85 Gal for East–West direction. Therefore, the amplification is highly polarized in the direction of East–West. We also show the Fourier spectrum of the input acceleration time series and response time series in Fig. 9a. The frequency content from 1 to 3 Hz is amplified in EW direction but de-amplified in NS direction. This amplification agrees well with the Fourier spectrum of original record for the 2-second portion around the time of PGA position in Fig. 9c. The amplification factor for EW component is decreased significantly from 3 to 4 Hz. This kind of decrease is also pronounced in the fourier spectrum of the recorded ground motion. Around the PGA position of the record, we computed the instantaneous frequency around the PGA position, and they are averaged to 8 Hz with 20 instantaneous frequency value around the PGA position. Figure 9a shows that the amplification factor of the frequency content around 8 Hz for EW component is much larger than the value of the NS component. From the ground motion recordings in Fig. 3, it also shows that the PGA value of EW component is much larger than the value of the NS component. Now we can conclude that the large PGA value in this station is mainly due to the topographic amplification.

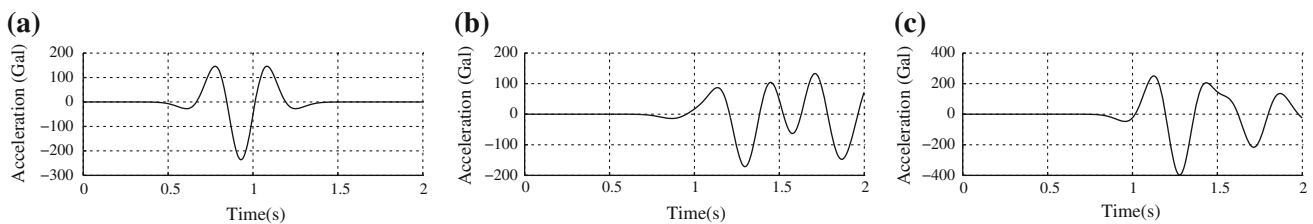


**Fig. 7** Input acceleration time series and the response time series at the station with  $f_p = 2$  Hz. **a** Input time series, **b** response in North–South direction by the polarized North–South shear wave, **c** response in East–West direction by the polarized East–West shear wave

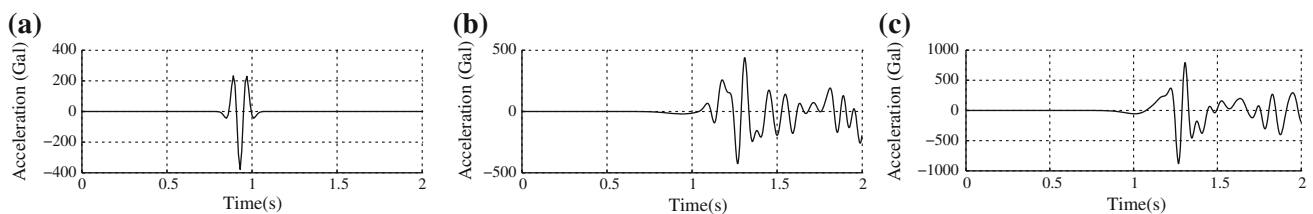


**Fig. 8** Input acceleration time series and the response time series at the station with  $f_p = 8$  Hz. **a** Input time series, **b** response in North–South direction by the polarized North–South shear wave, **c** response in East–West direction by the polarized East–West shear wave

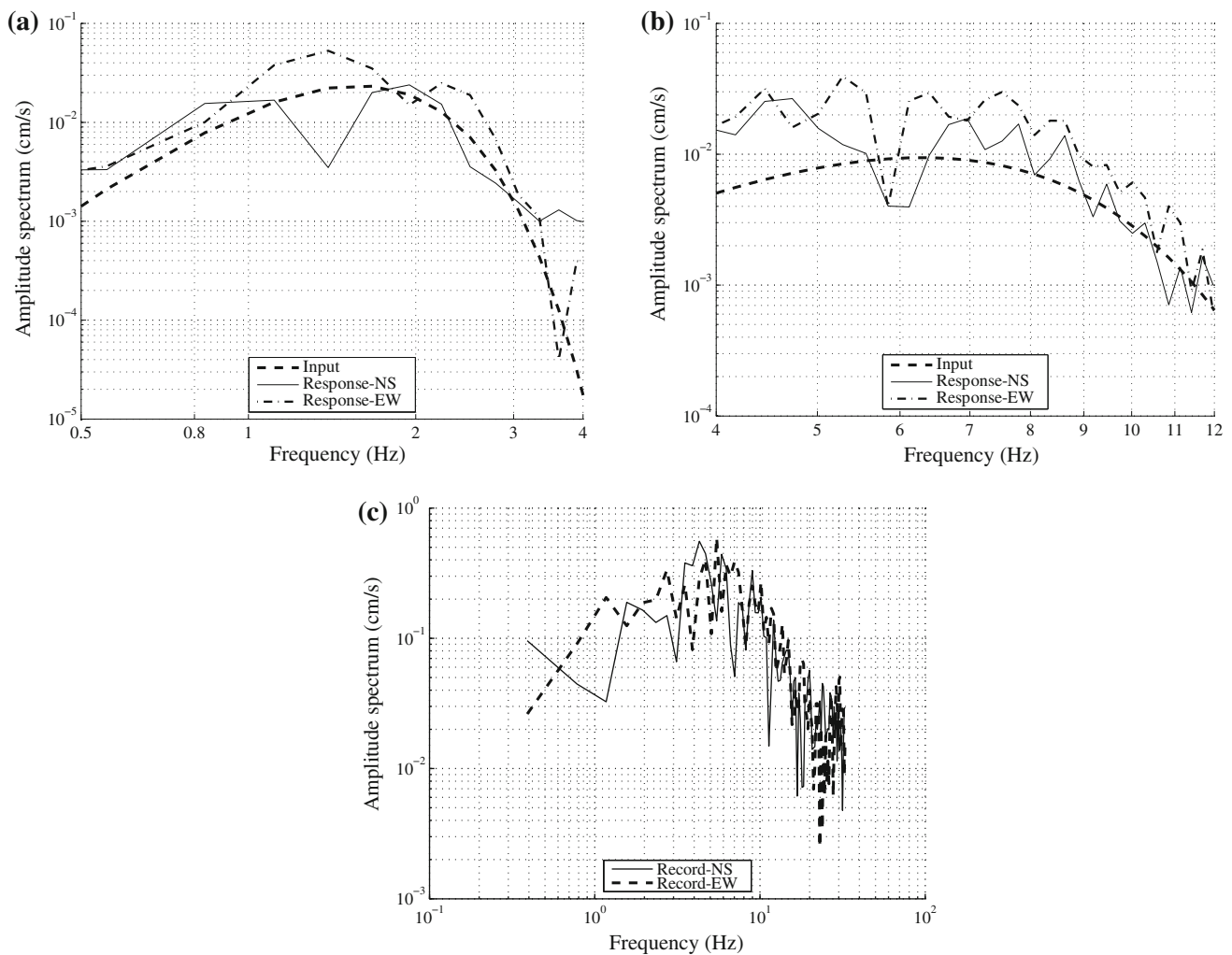


**Fig. 9** **a** The Fourier spectrum of the input acceleration time series and response time series with  $f_p = 2$  Hz. **b** The Fourier spectrum of the input acceleration time series and response time series with  $f_p = 8$  Hz. **c** The Fourier spectrum of the 2-second portion around the time of PGA position

The polarization due to topographic amplification also has been observed in some other earthquakes. Spudich et al. (1996) found the directional topographic site response at Tarzana in aftershocks of the 1994 Northridge earthquake.

#### 4 Conclusion

In our 3D SH wave simulation of the area, we have found that the amplification is polarized. Thus, buildings around this area should consider the max demanded orientation. The orientation of structure is a factor for the evaluation of aseismic level. The main frequency for the portion of large PGA value around the PGA position is about 8 Hz. Therefore, the main destructive energy of the ground motion is focused on high frequency. In the on site survey of the area around the 51BXD station, the damage is less

severe for tall buildings (natural period is long) compared with small buildings (natural period is short). This phenomenon is explained well by this study.

**Acknowledgments** This work was supported by the National Basic Research Program of China (2011CB013601), the National Natural Science Foundation of China (91215301, 61203276), and the Special Fund of the Institute of Geophysics, China Earthquake Administration (DQJB12B12).

#### References

- Assimaki D, Gazetas G, Kausel E (2005) Effects of local soil conditions on the topographic aggravation of seismic motion: parametric investigation and recorded field evidence from the 1999 athens earthquake. *Bull Seismol Soc Am* 95(3):1059–1089
- Bouchon M, Schultz CA, Toksöz MN (1996) Effect of three-dimensional topography on seismic motion. *J Geophys Res* 101(B3):5835–5846



- Chang K-H, Tsaor D-H, Wang J-H (2013) Scattering of SH waves by a circular sectorial canyon. *Geophys J Int*
- Gao Y, Zhang N, Li D, Liu H, Cai Y, Wu Y (2012) Effects of topographic amplification induced by a u-shaped canyon on seismic waves. *Bull Seismol Soc Am* 102(4):1748–1763
- Hartzell SH, Carver DL, King KW (1994) Initial investigation of site and topographic effects at robinwood ridge, California. *Bull Seismol Soc Am* 84(5):1336–1349
- Hough SE, Altidor JR, Anglade D, Given D, Janvier MG, Maharrey J Z, Meremonte M, Mildor BS-L, Prepetit C, Yong A (2010) Localized damage caused by topographic amplification during the 2010 *M*7.0 Haiti earthquake. *Nat Geosci* 3(11):778–782
- Iwahashi J, Kamiya I, Matsuoka M (2010) Regression analysis of *V*<sub>s30</sub> using topographic attributes from a 50-m DEM. *Geomorphology* 117(1–2):202–205
- Kaiser A, Holden C, Massey C (2013) Determination of site amplification, polarization and topographic effects in the seismic response of the port hills following the 2011 christchurch earthquake. NZSEE Conference, Wellington, New Zealand
- Komatitsch D, Tromp J (1999) Introduction to the spectral element method for three-dimensional seismic wave propagation. *Geophys J Int* 139(3):806–822
- Komatitsch D, Vilotte J-P (1998) The spectral element method: an efficient tool to simulate the seismic response of 2d and 3d geological structures. *Bull Seismol Soc Am* 88(2):368–392
- Spudich P, Hellweg M, Lee W (1996) Directional topographic site response at tarzana observed in aftershocks of the 1994 northridge, California, earthquake: implications for mainshock motions. *Bull Seismol Soc Am* 86(1B):S193–S208
- Tsaor D-H (2011) Scattering and focusing of sh waves by a lower semielliptic convex topography. *Bull Seismol Soc Am* 101(5):2212–2219
- Yong A, Hough SE, Iwahashi J, Braverman A (2012) A terrain-based site-conditions map of California with implications for the contiguous united states. *Bull Seismol Soc Am* 102(1):114–128
- Zhang N, Gao Y, Cai Y, Li D, Wu Y (2012a) Scattering of sh waves induced by a non-symmetrical v-shaped canyon. *Geophys J Int* 191(1):243–256
- Zhang N, Gao Y, Li D, Wu Y, Zhang F (2012b) Scattering of sh waves induced by a symmetrical v-shaped canyon: a unified analytical solution. *Earthq Eng Eng Vib* 11(4):445–460